Computational Design of Laser-Cut Bending-Active Structures

Emmanuel Rodriguez, Georges-Pierre Bonneau, Stefanie Hahmann, Mélina Skouras

Computational Design of Laser-Cut Bending-Active Structures

Emmanuel Rodriguez, Georges-Pierre Bonneau, Stefanie Hahmann, Mélina Skouras

Univ. Grenoble Alpes, INRIA, CNRS, Grenoble INP, LJK, France

Abstract

We propose a method to automatically design bending-active structures, made of wood, whose silhouettes at equilibrium match desired target curves. Our approach is based on the use of a parametric pattern that is regularly laser-cut on the structure and that allows us to locally modulate the bending stiffness of the material. To make the problem tractable, we rely on a two-scale approach where we first compute the mapping between the average mechanical properties of periodically laser-cut samples of mdf wood, treated here as *metamaterials*, and the stiffness parameters of a reduced 2D model; then, given an input target shape, we automatically select the parameters of this reduced model that give us the desired silhouette profile. We validate our method both numerically and experimentally by fabricating a number of full scale structures of varied target shapes.

Keywords: active bending, laser-cutting, metamaterial, inverse design, computational fabrication

1. Introduction

Bending-active structures are curved structures made of initially planar components that have been elastically bent so that they assume a 3D shape [1]. This construction technique offers several advantages: flat panels are easy to manufacture, store and transport, and can be used to create objects of multiple scales, from models to large-scale structures. These multiple benefits explain the popularity of active bending for design applications as well as in architecture [2, 3, 4].

In this work, we are interested in controlling the shapes of the silhouettes of bent planar strips of plywood. More specifically, we want the profile of the deformed structure, subject to external loads, to match a given target curve when at equilibrium. While this can be achieved by playing with the width of the strips (see e.g. the recent work by Hafner and Bickel [5]) or their thickness (at the expense of a more involved fabrication process), we do not want to alter the *outer* shape of our ribbons. Instead, drawing inspiration from the design of living hinges and from kerfing techniques used in lute-making, we propose to modulate the curvature of our structures by patterning their *interior* according to a parameterized rectangular motif that is regularly laser-cut. Inserting such cuts to the initially flat panel through laser-cutting is no more difficult than cutting its external layout. Our objects can thus be fabricated using a widespread, scalable and affordable technique.

On the computational side, relying on a parametric cut pattern allows us to treat the cut fiberboard as a *metamaterial* with programmable bending capabilities and to turn towards two-scale methods when solving the inverse design problem of finding cut parameters that will produce a bending-active structure with the desired target profile. To our knowledge, such an approach, leveraging explicit bending control and building on recent results in bending homogenization [6], has not yet been proposed in the context of computational fabrication.

While we focus on the particular setting of 2D structures and rectangular cuts, we believe that our technique, that decouples macro-scale geometry from material inner structure paves the way to generalization. Indeed, beyond the mechanics of the final object, the shapes of the cuts also impact its appearance. Therefore, playing with the cut patterns also allows to play with the aesthetics of the structure. Our methodology, which does not explicitly rely on a specific pattern geometry should be extendable to other motifs, as long as they form a parametric family and exhibit a wide range of mechanical behaviors.

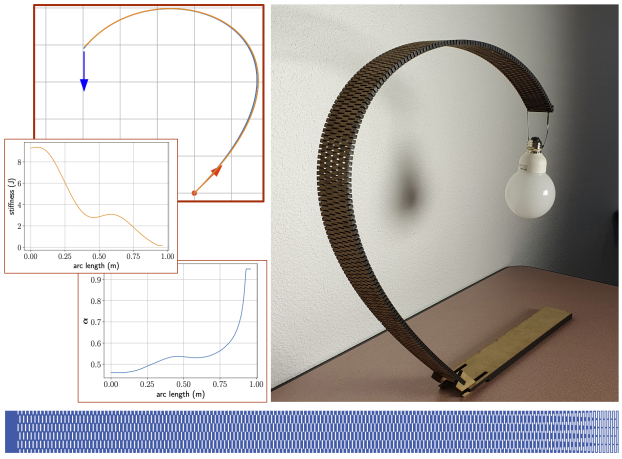

Figure 1: Plots from top to bottom: an input curve with prescribed boundary conditions and external forces, the optimized stiffness profile of the bending-active structure, the geometric parameters of the cutting patterns. Bottom: the cut layout. Right: the laser-cut bending-active structure whose silhouette matches the input target curve.

In summary, the main contributions of our work are the following:

- We propose a novel "living-hinge"-inspired *parametric* family of laser-cut metamaterials with tunable bending capabilities.
- We characterize the bending properties of these metamaterials using a recent bending homogenization method "with a twist".

Email addresses: melina.skouras@inria.fr (Mélina Skouras), georges-pierre.bonneau@inria.fr (Mélina Skouras)

- We present a two-scale algorithm for the inverse design of bending-active structures of custom deformed shape.

2. Related works

Fabrication-aware computational design has gained increasing interest in computer graphics for a decade. For a broad overview of the field, we refer the reader to the surveys by Bickel et al. [7] and Bermano et al. [8], which cover a wide variety of techniques. In the following section, we focus the discussion on previous work on inverse design of deployables and slender structures, metamaterials and Kirigami-inspired research.

Deployable surfaces. These structures share with ours that they are fabricated flat and assume a 3D shape once deformed. Existing fabrication techniques include the use of flat beams for weaved items [9, 10] and for gridshells [11, 12, 13], well adapted to large-scale structures, e.g., architectural installations, sealed inflatable membranes [14, 15] and 3D printed structures [16] for smaller scale models, wire meshes [17], as well as laser-cut rigid panels [18, 3] or softer elastic sheets [19, 20]. Common to all these approaches is that curvature is typically obtained from metric frustration. This is why the actual 3D structures generally exhibit non-zero Gaussian curvature and are doubly curved. By contrast, we are interested in controlling the *extrinsic* curvature of our strips, which cannot be achieved by modulating the surface metric alone.

Rods' design. Closer to our work are the approaches that address the inverse design of 2D and 3D rods and other slender structures so that they match a given target shape at equilibrium. For example, Derouet-Jourdan et al. [21] optimize the physical parameters of elasticæ to avoid sagging under gravity, and Bertails-Descoubes et al. [22] prove the uniqueness of the natural shape of the rods solution to the former problem. In the context of computational fabrication, Pérez et al. [23] control the bending stiffness of networks of rods by locally adjusting their cross-sections and rest centerlines. More recently, Liu et al. [24] explored the design of axis-symmetric structures formed by tapered ribbons. Their theoretical results were extended and generalized by Hafner and Bickel [5] who investigated the design space of planar elastic rods for form-finding applications. This latter work shares similarities with ours but also notable differences: on the fabrication side, bending control of the optimized strips is achieved by playing with their width, while we modify their inner meso-scale geometric structure; on the numerical side, this previous study is focused on clamped-clamped ribbons whose deformed shape is primarily determined by geometric boundary conditions, while we are also interested in structures able to carry external loading.

Metamaterials and two-scale approaches. In a broader context, a popular approach to design an object with a given target shape consists in modifying the structure of the object at a local scale, so as to tune its local geometric and mechanical properties [25, 26, 27]. For deployable surfaces, as the ones mentioned above, the intent is generally to be able to control the in-plane behavior of the surface; many related works thus exploit so-called auxetic metamaterials, i.e. engineered materials that can stretch, or contract, in all tangential directions simultaneously [18, 16, 20]. The use of structural patterns that are quasi-periodic has the big advantage of allowing for the use of multi-scale approaches when designing an inverse modeling tool. These methods typically proceed in two steps: the local macro-scale properties of the material are first homogenized; then they are used as parameters in an inverse problem [25, 28]. In this work, we also rely on this type of approach, but rather than exploiting the *in-plane* properties of the considered metamaterial, we play with its *out-of-plane* mechanical behavior. While some reduced models may indirectly capture the flexural resistance of the proposed metamaterials [16, 29], as far as we know, the only graphics works that explicitly looked into the homogenization of the bending behavior of structured material sheets are those by Schumacher et al. [30] and Sperl et al. [6]. In our work, we build on the latter to characterize the properties of our laser-cut plates. However, rather than applying the method to speed-up forward simulations, we investigate its use in the context of inverse design.

Kirigami. The fabrication technique that we leverage, based on the cutting of a relatively thin plate, is reminiscent from Kirigami, a Japanese art consisting in cutting and folding paper in order to create 3D surfaces. Kirigami has recently inspired several researchers from the material science community in the context of various applications, from the design of nano-structures of complex unfolded shapes [31, 32] to the one of metamaterials formed by thin sheets of material regularly cut according to a (quasi) periodic pattern [33, 34]. However, most previous work in the latter category, closest to our work, investigated the mechanical behavior of these metamaterials under tension, while we are interested in their bending response under non-axial loading.

3. Overview

Given a planar target curve, external planar forces and boundary conditions (Fig. 1, top-left), our method produces a bending-active structure made of a rectangular piece of wood panel in which holes are laser-cut (Fig. 1, right). The silhouette of the structure in physical equilibrium is aimed to match the target under the given loading conditions. The actual output of our process are the geometric parameters (Fig. 1, curve-plots) defining the cut layout (Fig. 1, bottom) which locally modulates the bending stiffness of the material.

Working on a full scale model, i.e. optimizing the geometry of the cuts in 3D directly, would be intractable. We therefore rely on an intermediate, reduced, 2D representation, and we solve an inverse problem involving the parameters of this reduced model. In practice, our approach involves three stages:

- building the reduced model (a discrete version of a 2D Kirchhoff rod, in our case) and mapping its parameters, here its mechanical properties, to the parameters of our original problem, i.e. the geometry of the cuts . We will do this by locally treating the cut wood as a parametric metamaterial and relying on an homogenization approach (Section 4);

- casting our original inverse design problem as a constrained optimization problem, whose unknowns are the parameters of the reduced model, i.e. its nodal bending stiffnesses (Section 5);

- mapping back the optimized structure's stiffness profile to cut patterns to infer the final cut layout.

We validate our algorithm by designing a number of bending-active structures, four of which have also been fabricated (Section 6).

4. Laser-cut metamaterial

Metamaterials are engineered materials designed to exhibit superior mechanical properties to those of the constituent material. They are structured with periodically arranged or spatially varying building blocks which either define a homogeneous, resp. heterogeneous metamaterial. Tailor-made geometry of the building blocks is the key for gaining extraordinary properties.

Designing a metamaterial, and characterizing its mechanical behavior, is not only a matter of geometry, but also of scale. In our setting, where bending-active structures are made of wood panels in which a geometric pattern of holes is laser-cut to tune the mechanical behavior, the latter is modeled at two scales: by a so-called *mesoscopic mechanical model* at the scale of material, which corresponds to a solid material with geometrically parameterized holes, and by a so-called *macroscopic mechanical model* at the scale of the complete object.

Furthermore, the models are simplified at 2 levels:

- At the material level: we approximate a *heterogeneous* structure made of solid material and geometrically parameterized holes by a *homogeneous* material having another material law.
- At the level of the representation of the full object: we approximate the geometry of a *3D* strip with *finite* thickness, i.e. a 3D object, by a *planar curve*. Indeed, we are interested in the silhouette of the ribbon, which has constant width and whose patterns remain periodic along the y axis. We therefore expect its motion to stay planar, which allows us to represent the final geometry by a 2D curve. We will model its mechanical behaviour using a Kirchhoff rod model.

We start by defining the geometric structure of our metamaterial and its parameters (Sect. 4.1) followed by the introduction of the mesoscopic and macroscopic mechanical models (Sect. 4.2 and 4.3). To investigate the macro mechanical behavior and link it to the material parameters of our rod model, we turn to numerical homogenization and explain how we handle periodicity (Sect. 4.4). In Sect. 4.5 we build the map from material parameters to geometric parameters.

4.1. Geometric structure

In designing the laser-cut patterns, we were inspired by numerous "living-hinge" examples and design tools [35]. A living-hinge can be loosely defined as a flexible piece of material connecting two planar rigid pieces of the same material along a line of hinge, so that the latter pieces can rotate around this line. Living hinges exploit indeed the natural tendency for material to bend around an array of cuts or notches. We choose one of the most standard cutting pattern used in living-hinges, in which rectangular holes are cut and arranged to form an alternating pattern, as illustrated in Fig. 2. Our bending-active structures act as beams where the longitudinal axis will be referred to as the x-axis and the transverse direction will be denoted y-axis. A structure of longitudinal dimension L_{struct} and transversal dimension W_{struct} is periodically cut. The periodic unit cell (dashed rectangle in Fig. 2) has dimensions $L_c \times 2W_c$. Note, that the longest dimension L_c of the unit cell is in the transverse direction of the whole structure. L_c (resp. W_c) is also the offset between rectangular cuts in the transverse (resp. longitudinal) direction. The rectangular cuts have dimensions $l_c \times w_c$. While L_c and W_c are constant throughout the whole structure, l_c and w_c vary in the longitudinal direction to be able to modify locally the bending stiffness. Instead of measuring these variations with the absolute values w_c and l_c in meters, we choose as design parameters the *adimensional* ratios $\alpha = \frac{l_c}{L_c}$ (transverse direction) and $\beta = \frac{w_c}{W_c}$ (longitudinal direction). α and β are spatially variable parameters, depending on the curvilinear x-abscissa (see Fig. 2). By varying α and β in the longitudinal direction we obtain beams which may be locally rigid (low values of α and β) or flexible (high values of α and β).

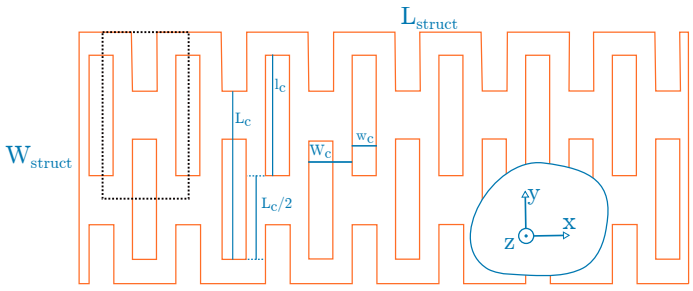

Figure 2: A bending-active structure of longitudinal dimension L_{struct} and transversal dimension W_{struct}. Dimensions and offsets of the rectangular cuts are shown in blue. The periodic unit cell is highlighted by a dashed rectangle. The main parameters in our design are the adimensional ratios $\alpha = \frac{l_c}{L_c}$ and $\beta = \frac{w_c}{W_c}$.

4.2. Mesoscopic mechanical model

In this Section we introduce the physical model which we choose to guide the mechanical behavior at the mesoscopic scale of our metamaterial. At this scale the meta-material is modeled in 3D with the geometry illustrated in Fig. 2, extruded in the z-direction.

Base material modeling. The constituent material we use for our physical realizations is MDF (Medium Density Fiberboard). MDF is a composite of fine, uniform wood fibers, which are bonded together by resins, heat and pressure. It is a heterogeneous material at the microscopic scale, and has a non-linear elastic behavior [36]. We approximate it as a homogeneous and isotropic material at the mesoscopic scale, using a standard Neo-Hookean material model with constitutive equation [37]

$$\Psi_{\text{Neo}} = \frac{\mu}{2}\left(\text{Tr}(\mathbf{C}) - 3\right) - \mu \log(J) + \frac{\lambda}{2}\left(log(J)\right)^2, \qquad (1)$$

where C is the right Cauchy-Green tensor, $J = \det(C)$ and λ, μ are the Lam coefficients, derived from the Young's modulus E and the Poisson's ratio ν using $\lambda = \frac{E\nu}{(1+\nu)(1-2\nu)}$ and $\mu = \frac{E}{2(1+\nu)}$. The Poisson's ratio is set to $\nu = 0.3$. Since bending is the most salient characteristic governing the deformation behavior in our application, we experimentally fit the Young's modulus with a cantilever test. In practice, we measured a deflection of 35 mm for a beam of length 79 cm and square section of 6 mm side, fixed at one of its ends, from which we deduced a Young's modulus of $E = 9.95$ GPa using the theoretical Euler-Bernoulli beam model.

Numerical model. When simulating the structure at the mesoscale, we need to numerically integrate the energy density (1). To this end, we discretize the 3D structure using `Gmesh` [38] with tetrahedral elements of typical edge size of 0.4 mm to 1.6 mm (exact figures are provided where appropriate) and solve the governing equations using the Finite Element solver FEniCS [39] with Lagrange elements of degree 2.

4.3. Macroscopic model

Because of our particular setting, where we want to reproduce 2D curves in the xz-plane, and the external forces are defined in the same plane, our bending-active structure behaves as a rod which deforms in this plane with no twist. Furthermore, since the primary mode of deformation of our structure should be bending, we assume that stretching can be neglected. Therefore at the macroscopic scale it is convenient to model our structure as a Kirchhoff rod in 2D, whose bending energy density (i.e. energy per unit length) is defined as

$$\delta E_b = \frac{1}{2} Y I \kappa^2,$$

where Y is the Young's modulus of the homogenized material, I is the second moment of area of the rod's cross section, and κ is the curvature of the rod [40].

For a rod with a rectangular cross-section bending with respect to the y axis (using the axis notations of Fig. 3), $I = \frac{1}{12} t^3 W$, where t and W are, respectively, the thickness of the rod and its width.

The total bending energy of a rod of length L is then

$$E_b^{\text{rod}} = \int_0^L \delta E_b dl = \int_0^L \frac{1}{2} Y I \kappa^2 dl,$$

i.e. E_b^{rod} is of the form

$$E_b^{\text{rod}} = \int_0^L \frac{1}{2} k_b W \kappa^2 dl, \quad \text{with} \quad k_b = \frac{1}{12} Y t^3. \tag{2}$$

Discrete model. In practice, we represent our rod using a simple sequence of linear and angular springs connecting the discrete nodes. The rod of length L_{struct} corresponding to our object profile is discretized into n nodes with position $\bar{\mathbf{x}}_i, 1 \leq i \leq n$, and $n-1$ edges $\mathbf{e}_i = \bar{\mathbf{x}}_{i+1} - \bar{\mathbf{x}}_i, 1 \leq i \leq n-1$. There are $n-2$ bending stiffnesses $k_b^i, 2 \leq i \leq n-1$, in Joule, assigned to each interior node. Following Bergou et al. [41], we discretize the rod's bending energy (2) as

$$E_{\text{bending}} = \sum_{i=2}^{n-1} \frac{1}{2} k_b^i W \frac{\|\kappa \mathbf{b}_i\|^2}{d_i^{\text{rest}}},$$

where W is the width of the structure, $d_i^{\text{rest}} = \frac{\|\mathbf{e}_{i-1}^{\text{rest}}\| + \|\mathbf{e}_i^{\text{rest}}\|}{2}$ is the Voronoi length of the interior node $\bar{\mathbf{x}}_i$ and $\kappa \mathbf{b}_i$ is the discrete curvature binormal vector given by (refer to [41] for more details):

$$\kappa \mathbf{b}_i = \frac{2 \mathbf{e}_{i-1} \times \mathbf{e}_i}{\|\mathbf{e}_{i-1}\| \, \|\mathbf{e}_i\| + \mathbf{e}_{i-1} \cdot \mathbf{e}_i}.$$

To model quasi inextensibility, we assign a linear spring to each edge with same elongation stiffness k_e, in Newton, set to a high value ($k_e = 1000$ N) and compute the discrete stretching energy of the rod as

$$E_{\text{stretching}} = \sum_{i=1}^{n-1} \frac{1}{2} k_e \frac{\|\mathbf{e}_i - \mathbf{e}_i^{\text{rest}}\|^2}{\|\mathbf{e}_i^{\text{rest}}\|}.$$

Finally, a mass m_i in kg is attached to each node in order to take into account gravity forces due to the structure itself. The total energy at the macroscopic level is then given by:

$$E_{\text{macro}} = E_{\text{stretching}} + E_{\text{bending}} + \sum_{i=1}^{n} g m_i z_i - W_{\text{ext. forces}},$$

where z_i is the height of $\bar{\mathbf{x}}_i$, $g = 9.81 \text{m s}^{-2}$, and $W_{\text{ext. forces}}$ is the work of the external forces.

By modifying the geometric parameters α, β along the longitudinal dimension (Section 4.1), we can adjust the values of the $n-2$ bending stiffnesses k_b^i of the macroscopic model, and thus control the shape at equilibrium $\bar{\mathbf{x}} = (\bar{\mathbf{x}}_1, \cdots, \bar{\mathbf{x}}_n)$ which is a solution of:

$$\bar{\mathbf{x}} = \underset{\bar{\mathbf{x}}_i}{\text{argmin}} \, E_{\text{macro}} \quad \text{s. t.} \quad \text{boundary conditions.} \tag{3}$$

In the next section 4.4 we will explain how to compute the bending stiffnesses k_b^i from the longitudinally varying geometric parameters α, β.

Forward modeling refers to the process of manually tuning the geometric parameters α, β, and solve (3) until the input shape is reproduced with satisfaction. We have implemented the solution of (3) using the optimization library `IPOPT` [42], in order to quickly test different design ideas in terms of boundary conditions and external forces.

In Section 5 we will invert this process, and automatically find the geometric parameters allowing to reproduce the input shape.

4.4. Homogenization

In this Section we explain how to compute the mapping from the geometric parameters α, β of the model at the mesoscopic scale, to the bending stiffnesses k_b of the model at the macroscopic scale. Such a mapping between parameters at mesoscopic and at macroscopic scale can be derived through the framework of numerical homogenization.

The main idea of numerical homogenization is to determine effective macroscopic mechanical properties, such as the elasticity tensor, based on representative simulations of a periodic unit cell at mesoscopic scale (theoretical foundations in [43, 44]). Application of numerical homogenization in our case is closely related to that of [30, 6], where periodic boundary conditions for the case of thin shell bending deformation have been considered. We follow the notations of [6]. $\mathbf{X}$ is a position at mesoscopic scale and at rest. $\mathbf{x}(\mathbf{X})$ is the position after deformation. The theory of homogenization assumes that at any point of a deformed material observed at a macroscopic scale, there exists a mesoscopic scale representation, valid in a representative volume element (RVE), centered around the point. This representation expresses the points (at mesoscopic scale) $\mathbf{x}(\mathbf{X})$ as the sum of a first order approximation of the macroscopic deformation, and a mesoscopic scale displacement fluctuation $\tilde{\mathbf{u}}(\mathbf{X})$. Two conditions must be fulfilled by $\tilde{\mathbf{u}}(\mathbf{X})$. The first condition is the averaging constraint $\int_{\text{RVE}} \tilde{\mathbf{u}} = 0$, which intuitively states that the local fluctuations average out at the macroscopic scale. The second condition is the periodicity constraint $\tilde{\mathbf{u}}^+ = \tilde{\mathbf{u}}^-$ which states that the local fluctuation takes the same values on both sides of the RVE. In other words, periodic copies of the locally displaced RVE join continuously.

Bending homogenization. In the case of a bending deformation, the two-scale representation can be stated as follows, analogously to [6]:

$$\mathbf{x}(\mathbf{X}) = \mathbf{R}_\theta(\mathbf{X}) + \tilde{\mathbf{u}}(\mathbf{X}), \tag{4}$$

where $\mathbf{R}_\theta(\mathbf{X})$ denotes the bending deformation observed at the macroscopic scale. Fig. 4-middle shows a schematic illustration of this decomposition. Fig. 3 shows the RVE at rest (dashed

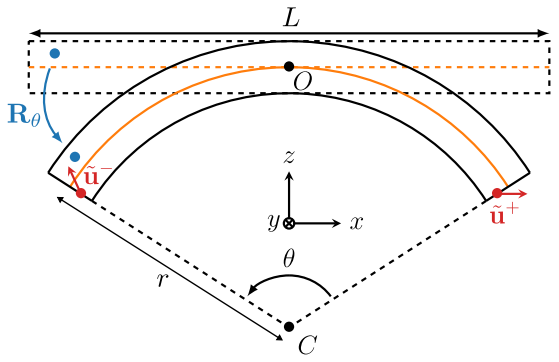

Figure 3: The bending transformation $\mathbf{R}_\theta$ applied to the RVE.

rectangle) and deformed by $\mathbf{R}_\theta$. The amount of bending is parametrized by the angle θ. Referring to Fig. 3, a RVE of longitudinal dimension L, bent by an angle $\theta > 0$, has a constant radius of curvature $r = \frac{L}{\theta}$. The RVE is composed of adjacent periodic unit cells (dashed rectangle in Fig. 2). Choosing the RVE too small would result in overconstraining the local fluctuations $\tilde{\mathbf{u}}$. On the other hand, choosing it too large increases the computational time quickly. Using the method explained below, we computed $\tilde{\mathbf{u}}$ for increasing size of the RVE and found that beyond a size of 2 unit cells in longitudinal direction, and 1 unit cell in transverse direction, negligible difference is observed between the successive displacement functions. Therefore, we choose a RVE of size $L = 4W_c$ in longitudinal direction, L_c in the transverse direction, and t in the z-direction (t is the thickness of the wood panel). With these notations, the macroscopic bending deformation $\mathbf{R}_\theta$ is given by:

$$\mathbf{R}_\theta : \mathbf{X} = \begin{pmatrix} X \\ Y \\ Z \end{pmatrix} \rightarrow \mathbf{R}_\theta(\mathbf{X}) = \begin{pmatrix} (\frac{L}{\theta} + Z)\sin(\frac{X\theta}{L}) \\ Y \\ (\frac{L}{\theta} + Z)\cos(\frac{X\theta}{L}) - \frac{L}{\theta} \end{pmatrix}$$

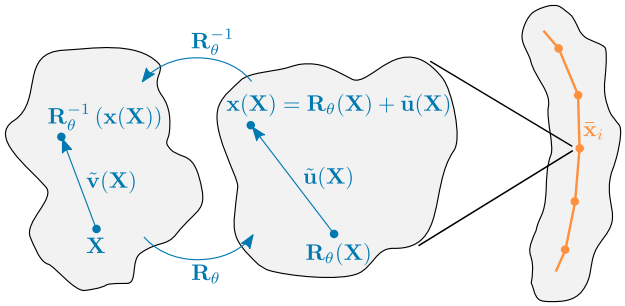

Figure 4: The local displacement fluctuation $\tilde{\mathbf{u}}$ of the RVE is mapped to a local displacement fluctuation $\tilde{\mathbf{v}}$ in a computational domain. This mapping allows to simplify the periodic boundary conditions (6) and the averaging constraints (7).

As pointed out by [6], the averaging and periodicity constraints on the local fluctuations $\tilde{\mathbf{u}}$ must be adapted to ensure these fluctuations average out properly when applied to a bent RVE. Therefore [6] introduces co-rotated periodicity conditions and averaging constraints. While following a similar approach, we map the two-scale representation (4) to a computational domain, and express the averaging and periodicity conditions in this domain. Referring to Fig. 4, we define a new displacement field $\tilde{\mathbf{v}}$ by:

$$\tilde{\mathbf{v}}(\mathbf{X}) = \mathbf{R}_\theta^{-1}\left(\tilde{\mathbf{u}}(\mathbf{X}) + \mathbf{R}_\theta(\mathbf{X})\right) - \mathbf{X}$$

The two-scale representation (4) maps to:

$$\mathbf{R}_\theta^{-1}(\mathbf{x}(\mathbf{X})) = \mathbf{X} + \tilde{\mathbf{v}}(\mathbf{X}). \tag{5}$$

In other words, $\tilde{\mathbf{v}}$ displaces points at rest ($\mathbf{X}$) while $\tilde{\mathbf{u}}$ displaces $\mathbf{R}_\theta(\mathbf{X})$. In the computational domain the co-rotated periodicity conditions on $\tilde{\mathbf{u}}$ can be expressed as simple periodicity conditions (6) on $\tilde{\mathbf{v}}$. And the co-rotated averaging constraints on $\tilde{\mathbf{u}}$ are expressed as simple averaging constraints (7) on $\tilde{\mathbf{v}}$. This simplifies the implementation since standard FEM libraries have built-in capacities for handling periodic finite element basis functions, fulfilling (6).

$$\tilde{\mathbf{v}}^+ = \tilde{\mathbf{v}}^- \tag{6}$$

$$\int_{\text{RVE}} \tilde{\mathbf{v}} = 0. \tag{7}$$

Finally, we can now compute the local fluctuations $\tilde{\mathbf{v}}$, and the potential energy $E_b^{3D}(\theta)$ of the deformed RVE, by solving the following static equilibrium problem: at (6) and (7) are satisfied.

$$E_b^{3D}(\theta) = \min_{\tilde{v}} \int_{\text{RVE}} \Psi_{Neo}(\tilde{v}), \tag{8}$$
$$\text{s. t.} \quad (6) \text{ and } (7) \text{ are satisfied.}$$

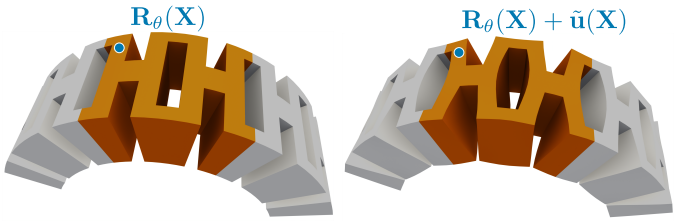

Figure 5: Bending homogenization. The left figure shows the cylindrical deformation $\mathbf{R}_\theta(\mathbf{X})$ of three RVEs. The right figure shows in orange the central RVE deformed periodically by the mesoscopic displacement fluctuations $\tilde{\mathbf{u}}$.

Computing the bending stiffness of the reduced model. As mentioned in Section 4.3, the bending term of our reduced model discretizes that of a Kirchhoff rod that reads

$$E_b^{\text{rod}} = \int_0^L \frac{1}{2} k_b W \kappa^2 dl$$

in the continuous setting.

Therefore, the bending energy of a deformed rod with uniform curvature $\kappa = \frac{1}{r}$ and constant stiffness k_b is

$$E_b^{\text{rod}} = \frac{1}{2} k_b W \frac{1}{r^2} L.$$

Denoting by θ the opening angle of the arc formed by the rod (see Fig. 3), E_b can be rewritten as a quadratic function of θ as

$$E_b^{\text{rod}}(\theta) = \frac{1}{2L} k_b W \theta^2,$$

since, in that case, $L = r\theta$.

Our goal is to estimate, for each considered (α, β) pair, the bending stiffness k_b of the reduced model that will best capture the macro-scale mechanical behavior of the corresponding laser-cut strip of wooden MDF. We do so by matching, in the least square sense, the energies E_b^{rod} and E_b^{3D} of the two models corresponding to bending deformations of increasing curvature, gravity turned off, i.e. we find the optimal $\tilde{k_b}$ defined by

$$\tilde{k_b} = \underset{k_b}{\text{argmin}} \frac{1}{2} \sum_i (E_b^{\text{rod}}(\theta_i) - E_b^{\text{3D}}(\theta_i))^2 = \frac{\sum_i a_i E_b^{\text{3D}}(\theta_i)}{\sum_i a_i^2}, \tag{9}$$

where $a_i = \frac{1}{2L} W \theta_i^2$ and the (θ_i) are to the opening angles corresponding to these deformation tests.

In practice, we consider RVEs of two unit cells in length that we bend up to a maximum angle of $\theta_{max} = 0.2$ rad. For unit cells of width $W_c = 3$ mm like ours, this corresponds to a radius of curvature of 3 cm, which is enough for our application. We define (θ_i) as a uniform sampling of $[0, \theta_{max}]$ using 11 values.

As shown in Fig. 6, left, the Kirchhoff rod model captures well the behavior of the cut 3D plates for a wide range of bending deformations.

4.5. Building the map from bending stiffnesses to geometric parameters

We initially considered varying both the relative length α and width β of our cut pattern. In practice, to explore the range of achievable bending stiffnesses, we uniformly sampled α and β between 0.3 and 0.9, using increments of 0.05, and we estimated the corresponding k_b using a relatively coarse 3D mesh (edge size of 1.6 mm) (see Fig. 6, middle). Noting that the length of the cuts had a much bigger impact on the structure's bending stiffness than the cuts' width, we then decided to keep β fixed and to play with the α value only. We set β to 0.6, the middle of the original sampled range and recomputed the bending stiffnesses using a finer sampling for α (increments of 0.01) and a finer discretization for the 3D meshes (maximum element size of 0.4 mm), for a total of about 50k to 100k elements (the maximum that would fit in the memory of our computer), depending on the α value (Fig. 6, right). In practice, to compute one value of bending stiffness $\tilde{k_b}$ we need to solve 11 times problem (8). This process takes between 1h to 5h with these mesh dimensions (see Section 6.1 for the specification of our computing platform). All values of k_b are computed and stored as a pre-process.

Despite a bit of noise for small values of α, i.e. for highly rigid materials (likely due to high sensitivity to the mesh discretization in this regime), we observe that the bending stiffness k_b strictly decreases as the length of the cut increases, as one would expect. This allows us to invert the relation and to build the map from stiffness to geometric parameter, $\alpha(k_b)$, by linearly interpolating the computed k_b values, after smoothing the latter thanks to a basic Gaussian filter (average of immediate neighbours), applied five times (see Fig. 6, right).

5. Inverse design algorithm

We now address an inverse design problem for laser-cut MDF panels. Remember our initial problem: given a 2D target profile shape and user-defined external forces and boundary conditions, we are searching for a cut layout of a planar panel of fixed length and width, such that the silhouette of the deformed panel matches the target under physical equilibrium.

The approach for solving this inverse modeling problem consists of two main steps. First, a constrained optimization problem is solved to find the nodal stiffness values and node positions of the reduced model at physical equilibrium matching the profile curve. Second, the optimized stiffness values are mapped back to the cut pattern parameters to infer the final cut layout.

In addition to the target curve, the user determines the boundary conditions. Our current implementation (see Section 4.3) enables to prescribe fixed points, tangent vectors at any point, individual spring stiffnesses and a mass added either at one end point or at one interior point, but can be extended to others.

5.1. Optimization of the stiffness profile

The purpose of the first step of our inverse modeling approach is to compute simultaneously the deformed shape and the corresponding stiffness values best approximating the target shape. We formulate this inverse design problem in a constrained optimization framework. The target shape is assumed to be a smooth curvature continuous shape equidistantly sampled as a 2D polygonal curve T whose n vertices are denoted by $\bar{\mathbf{x}}_t \in I\!R^{2n}$. The variables to be optimized are the vertex positions of the deformed object $\bar{\mathbf{x}}$ and the material stiffness values at macro scale $\mathbf{k}_b$. The objective function Φ to be optimized is a combination of three metrics defined in the following:

$$\min_{\mathbf{k}_b, \bar{\mathbf{x}}} \Phi_{\bar{\mathbf{x}}_t}(\mathbf{k}_b, \bar{\mathbf{x}}) \quad \text{s.t. } \nabla E_{\text{macro}} = 0 \text{ and } k_{min} \leq \mathbf{k}_b \leq k_{max} \quad (10)$$

where $k_{min} = 0.19$ J and $k_{max} = 60$ J in our implementation. The lower bound of $\mathbf{k}_b$ is provided by the maximal feasible cut size. Indeed, the bigger α is, the closer the cuts are to each other and the more the bending stiffness decreases (see Fig. 6, right). The material risks to break. We set $k_{min} = 0.19$ J, which corresponds to less than 1 mm material left between the holes, i.e. $\alpha = 0.95$. The upper bound is set by the maximal bending stiffness reached for the full material.

Shape similarity. The main role of the objective function Φ is to ensure that the final shape best matches the target shape. We encode fidelity to the target shape by relating the curvature values, instead of the curves themselves. This approach follows the idea that curvature is not only an intrinsic shape descriptor, but is known as an efficient shape similarity measure [45, 46, 47], since local 2D curvature is a highly informative visual cue for global shape perception, object recognition, and image interpretation [48]. The local curvature similarity between the deformed shape and the target shape is defined as

$$\Phi_{\text{similarity}} = \|\mathbf{c}(\bar{\mathbf{x}}) - \mathbf{c}(\bar{\mathbf{x}}_t)\|^2_{I\!R^n},$$

where $\mathbf{c}(\bar{\mathbf{x}})$ is a linearized discrete curvature vector at $\bar{\mathbf{x}} = [\bar{\mathbf{x}}_1, \ldots, \bar{\mathbf{x}}_n]$ with $\mathbf{c}(\bar{\mathbf{x}}_i) = (\bar{\mathbf{x}}_{i+1} - 2\bar{\mathbf{x}}_i + \bar{\mathbf{x}}_{i-1}) / \|\bar{\mathbf{e}}_i\|^2$. We divide by the squared length of the curve segment to achieve scale independence. In addition to enforce shape similarity, this penalty function also acts as a regularization term, since the target shape is assumed to be a smooth curvature continuous curve.

Distance to target. Euclidean distance between corresponding curve vertices cannot be ignored completely, because it prevents the curves to shift and rotate from each other. Indeed, two planar curves with same curvature vector are identical up to a translation. We therefore add a distance penalty defined as

$$\Phi_{\text{distance}} = \|\bar{\mathbf{x}} - \bar{\mathbf{x}}_t\|^2_{I\!R^n}$$

and assign it a very small weight.

Minimal stiffness variation. In addition to the geometric shape, we are searching for optimal bending stiffness. However, a regularization of the stiffness values is required in order to produce a smoothly varying geometric cut pattern (see Sect. 5.3). The latter is a necessary condition for the homogenization approach to be valid. We therefore introduce the following regularization penalty term

$$\Phi_{\text{regularization}} = \sum_{i=2}^{n-1} | \, k_b^{i-1} - 2k_b^i + k_b^{i+1} \, |^2.$$

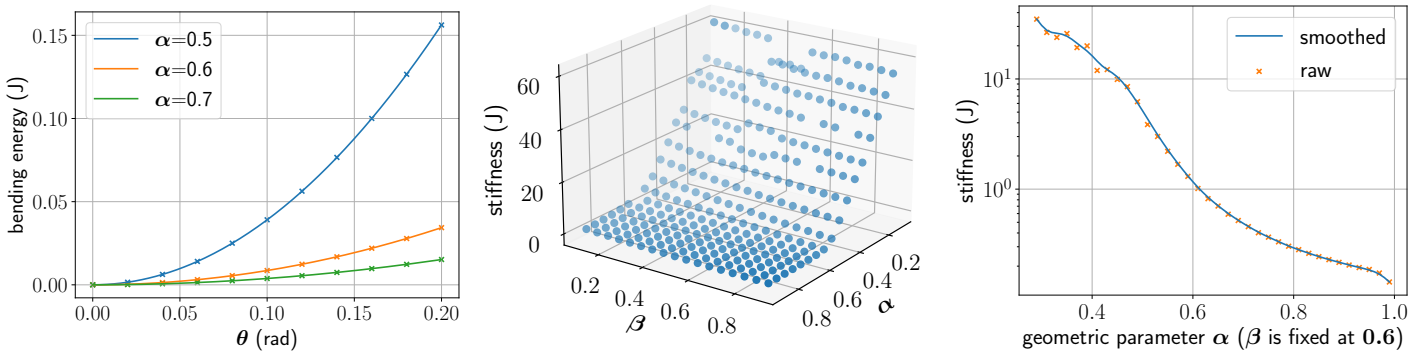

Figure 6: Left: Potential energy of the RVE with geometric parameters $\alpha \in \{0.5, 0.6, 0.7\}$, $\beta = 0.6$, for bending angle between 0 and 0.2 radians. Middle: stiffness according to α and β. Right: stiffness according to α with $\beta = 0.6$ (logarithmic scale to enhanced small values of stiffnesses).

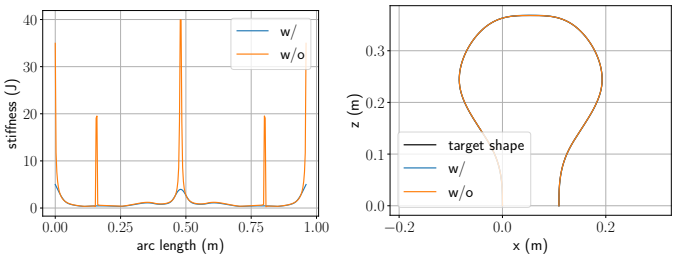

Figure 7: Optimized stiffness values computed w and w/o regularization.

Fig. 7 illustrates with an example that regularizing the stiffness even with a small weight is efficient and does not significantly alter the distance between the deformed shape and the target.

In summary, the objective function writes

$$\Phi = \omega_1 \Phi_{\text{similarity}} + \omega_2 \Phi_{\text{distance}} + \omega_3 \Phi_{\text{regularization}}.$$

In all our examples we have set $(\omega_1, \omega_1, \omega_3) = (10^4, 10^{-2}, 10^{-2})$.

To solve (10) numerically, we use the open source software `IPOPT` [42], which implements an interior point optimization method to find a local solution.

The quasi-Newton BFGS implementation of `IPOPT` is applied. We need to compute the gradient of the energy E_{macro} (equality constraint in (10)), and its Hessian (Jacobian of the equality constraint). In our current setting, we only consider point masses as external forces, therefore the gradient and the Hessian of $W_{\text{ext. forces}}$ are trivial to compute, but more complex external forces could be taken into account.

The optimization problem (10) is non-linear and non-convex, so that the result depends on an initial guess of the variables $\bar{\mathbf{x}}$ and $\mathbf{k}_b$.

What works well in the present setting is to start from the target curve as initial guess for $\bar{\mathbf{x}}$ and set the bending stiffness uniformly to a constant value 5.14 J, corresponding to $\alpha = 0.5$. With this choice the optimization starts at the minimum of the objective function Φ but the important physical equilibrium constraint $\nabla E_{\text{macro}} = 0$ is not satisfied at the beginning. Alternatively we tried starting with the same uniform initial stiffness, and with $\bar{\mathbf{x}}$ set as the physical equilibrium (solution of (3)). We also tried to set the initial $\bar{\mathbf{x}}$ as the target curve, and to compute the stiffnesses minimizing E_{macro} (which is a linear problem to solve). But we found the first approach generally finds a better local minimum of Φ.

5.2. *Mass density adjustment*

Cutting the material results in a significant loss of mass

$$\bar{\rho}(\alpha, \beta) = \rho \cdot (1 - \alpha \cdot \beta),$$

where ρ is the mass density of the material without cuts and $\bar{\rho}$ the homogenized mass density of the cut material. As an example, for a cut with $\alpha = 0.5$ and $\beta = 0.5$, a quarter of the material is removed. It is therefore important to solve the inverse design problem (10) by taking into account the correct mass density of the structure.

Remember that E_{macro} in (10) is the *total potential energy* of the system, composed of internal energy, work of external forces and gravitational energy, that depends on the mass density of the structure. The correct mass density however depends on the amount of material to be cut-off following the cut parameters, which are only known at output of the system. It is therefore not possible to know exactly in advance the mass density of the output structure.

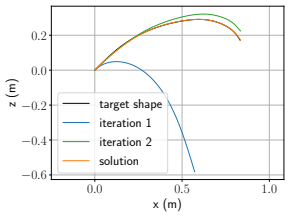

To solve this mass adjustment problem we implement an iterative mass reduction algorithm, which iterates the inverse modeling step until convergence on the nodal masses, see Algorithm 1. In practice, it is observed that the difference in masses quickly becomes smaller than 1% after 2 iterations. The inset shows the result of the forward simulation of the output of inverse modeling after taking into account the mass reduction. For this example our algorithm converges in 3 iterations.

Alternatively, we could parameterize the density by the stiffness parameters since the density depends on the size of the cuts (linear relation) and we know the relation between the size of the cuts and the stiffness parameter (piecewise linear relation - so not C^1). However, this would mean that we introduce a non-smooth term in the optimization problem. It is well known that this kind of non-regular minimization problem is much more difficult to solve than a problem for which the objective and the constraint are both differentiable. We therefore prefer to proceed in two steps in alternation, which allows us to use a standard gradient-based optimization method.

Algorithm 1 iteration on mass adjustment

Require:

function Mapping : $(\mathbf{k}_b) \mapsto (\alpha, \beta)$ ▷ $\mathbf{k}_b$ bending stiffnesses, ▷ (α, β) geometric parameters

InverseModeling : $(\mathbf{m}, T) \mapsto (\mathbf{k}_b)$ ▷ $\mathbf{m}$: list of nodal masses, ▷ T : (target shape, boundary conditions)

Mass : $(\alpha, \beta) \mapsto m(1 - \alpha\beta)$ ▷ m initial mass when no cuts

$\mathbf{m}_0 \leftarrow 0$

$\mathbf{m}_1$ = list of nodal masses

while $\|\mathbf{m}_0 - \mathbf{m}_1\|_2 \geq \varepsilon$ **do**

$\mathbf{k}_b$ = InverseModeling($\mathbf{m}_1, T$)

(α, β) = Mapping($\mathbf{k}_b$)

$\mathbf{m}_0 \leftarrow \mathbf{m}_1$

$\mathbf{m}_1 \leftarrow$ Mass(α, β)

end while

In order to compute the masses from the geometric parameters α, β we need to know the mass density of the MDF wood panels we are using. We measured the mass density by cutting a piece of known size and weighing it with a precision balance and obtained a density of 878 kg · m^{-3}.

5.3. Cut layout generation

Up to now, we have computed the discrete stiffness parameters of a reduced 2D model that, at equilibrium, closely matches the structure in target pose (Sect. 5.1). We therefore have a piecewise linear relation from arc length of our 2D model to bending stiffnesses.

The goal of this step is now to match the computed stiffness profile with geometric parameters for the cuts. We do this by directly reading the value of α corresponding to the curvilinear abscissa (x-value in Fig. 2) of the mid-point of each cut, using the map built in Section 4.5. In practice, the length of the edges of our discretized rod coincide with the width $2W_c$ of a unit cell so that the α that we compute are exactly those that correspond to the k_b values that we have optimized. See an example in Fig. 8.

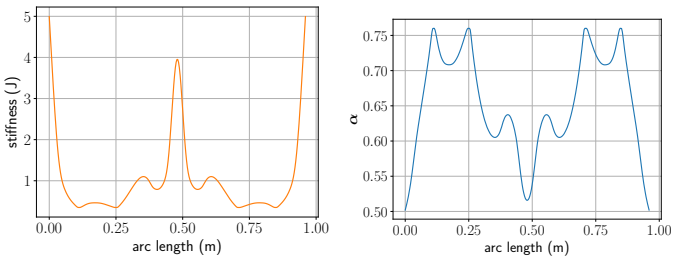

Figure 8: Optimized stiffness (left) computed with Eq. (10) and the corresponding α cutting parameters cutting parameters for 320 unit cells of width 3 mm (right) taken from the light bulb structure shown in Fig. 10(a).

6. Results

We have used our design system to create a diverse set of bending-active structures whose silhouettes at equilibrium match different target shapes. We demonstrate the versatility of our system by combining the target shapes with various sets of boundary conditions and external loads. In addition to computing numerous results, we have fabricated four structures in order to validate the presented design system as well as the choices and hypothesis made in Sections 4 and 5.

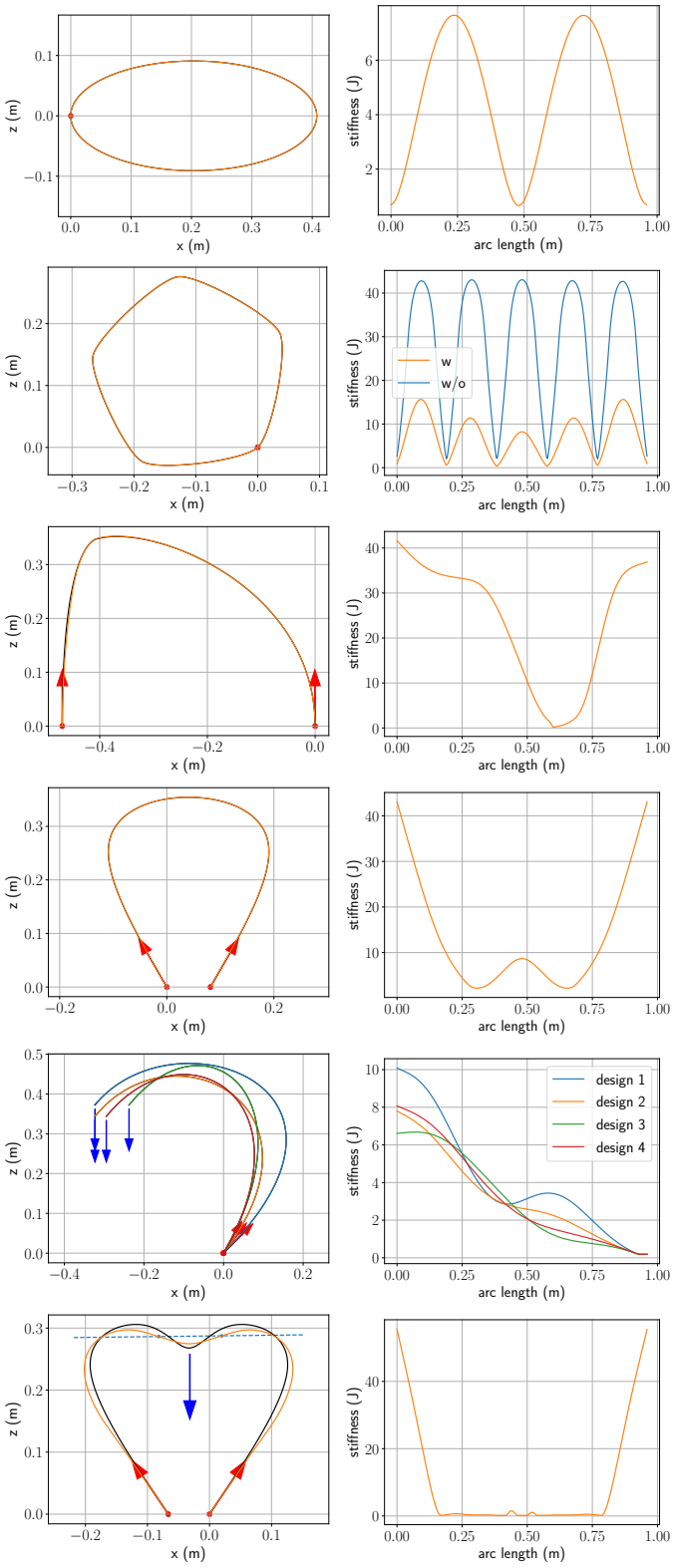

Figure 9: Computed bending-active structures (left) and stiffness profiles (right) generated from input shapes and boundary conditions. Input target shape (black), computed bending-active silhouette curve (orange). Boundary conditions (if applied) include fixed points (red dot), fixed tangent vectors (red arrow), external load (blue arrow) of 0.5 kg for the heart example. The ellipse and the pentagon (lines 1,2) are computed without taking gravity into account. The pentagon's stiffnesses have been computed with and without regularization. The bass clefs (line 5) result from 4 different target curves and an external load of 150 g.

6.1. Bending-active structures

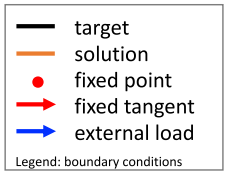

We showcase a variety of bending-active structures in Figures 9, 10 and 11. In addition to various shapes with partly strongly varying curvature profiles, we experimented with various sets of boundary conditions (BC) and external loads. The inset shows the legend for the boundary conditions as indicated in the figures throughout the paper. Table 1 summarizes all model statistics.

Experiments were run on a Dell Latitude 5410 (2020) with Intel Core i7 processor running at 4GHz with 16GB RAM.

In Fig. 9 shows the direct output of the inverse design problem (10). In the left column, the target curves $\bar{\mathbf{x}}_t$ (black) are superposed by the optimized curves $\bar{\mathbf{x}}$ (orange). The maximal relative distance to target (see Table 1) ranges from 0.01% to 0.2% for all examples, except for the heart with 1.2%. The right column shows the optimized stiffness profiles $\mathbf{k}_b$. The cut-layouts α_i for each unit cell are then taken directly from the stiffness profile via the monotone inverse mapping described in Section 5.3. We do show a few layouts for other examples in Fig. 10.

Robustness with respect to the boundary conditions has been studied in row 5 of Fig. 9. A set of 4 similar target curves (cubic B-splines) have been created. The BC for each curve consist of only one fixed point and tangent at the bottom extremity and an extra load of 150 g attached at the other. The algorithm converges well in all case. The asymmetric arch (row 3 in Fig. 9) showcases an example, where the BC are symmetric, but not the shape.

Target shapes. It is important to know from the beginning if a given target curve is *feasible*. Similar to [5], we say that a target shape is "feasible" if there is a solution to the constrained minimisation problem for which the distance to the target curve is close to 0. In our case however, feasibility does not imply *fabricability*, meaning that the structure will not break during bending. Although we have specified limits on the stiffnesses to avoid this failure, these limits are not a theoretical guarantee. In order to prevent failure during bending, we therefore derive an empirical link between the target's geometry and the optimized stiffnesses by observing above which curvature different laser-cut panels break during bending. To this end, we have constructed 6 panels of 50 cm in length, each with a uniform cut layout corresponding to $\alpha \in \{0.4, 0.5, 0.6, 0.7, 0.8, 0.9\}$, and bent them around cylinders with decreasing radius of curvature until the panel broke. The critical curvature values $\kappa_{critical}(\alpha)$ we found are $\{5, 6.7, 8, 25, 40, 50\}$ cm^{-1}. As a conclusion, we tag a target shape as *fabricable*, if none of its curvatures exceeds the critical value $\kappa_{critical} = 50$ cm^{-1} (i.e. none of its curvature radii is lower than 2 cm = 1/50).
The examples presented below all satisfy the maximal curvature constraint, except the heart with $\max(\kappa) = 56$ cm^{-1}, see Table 1 and discussions below. This fabricability test can be done in real-time and provides immediate feedback to the designer.

Once the algorithm converged to a solution $(\bar{\mathbf{x}}, \mathbf{k}_b)$ with a cut profile α it can further be checked if the curvatures of the individual panel elements (unit cells) with same cut parameters α satisfy $\kappa(\alpha) < \kappa_{critical}(\alpha)$. Here again, we observed with all examples, that the curvatures of resulting curves never exceed those of the target, in particular when the regularization term is switched on in the objective function (see pentagon example in Fig. 9).

With the heart shape in Fig.9, the method converges to a minimum energy curve and optimal stiffnesses within the prescribed bounds, even though the distance to target is not close to zero (1.2% error). Note our examples with an extra load extend the set of equilibrium curves considered in [5]. In particular the heart, where the line spanned by the 2 inflection points (dotted line) does intersect the equilibrium curve in 2 further points (see Fig.5 in [5]).

Choice of external load. The feature offered by our system to add external forces to a point on the structure extends the shape space of feasible shapes, see for example a mass added at the end of the bass clefs or at the mid point of the heart. In order to choose a mass which is not too large (danger of rupture) and not too small (difficulty to reach the target), we checked by forward simulation that the z-coordinate of the target loaded point is between the z-coordinate of this point if we were using the solid material and the z-coordinate of this point if we were using the softest material.

6.2. Fabricated prototypes

To further validate our approach, we constructed some physical prototypes. We use a Trotec Speedy 400 laser cutting machine, which allows for cutting sheets with maximal length of 1 m and maximal thickness of 6-10 mm (for MDF). The four bending-active structures we realized are made of MDF panels of 100 cm length and 6 mm thick. Panels with these dimensions withstand a large interval of cut pattern sizes without falling apart even when a reasonable amount of mass is added to its own mass.

Our idea was to realize lamp stands of original curved shapes. The complete set of data and obtained results are shown in Fig. 10. The designs from left to right represent (a) a light bulb, (b) an arch, (c) a desk lamp in form of a bass clef, and (d) a wall lamp. The four target shapes and the BC are shown in Fig. 10-top. The first 2 examples have symmetric BC at both extremities and a symmetric target shape. With the examples (c) and (d) we created the more challenging case where only one extremity is fixed and the other is only constrained by an extra load of 150 g. The bass clef and wall lamp examples are more challenging, because of the floating end point. We observed, that achievement of the target is sensitive to a proper choice of the extra mass. In Table 1, wee see that for both examples, the algorithm converged and computed $\min(\mathbf{k}_b) = 0.19$ J, which corresponds to large α-values, i.e. to coarse cut patterns.

The cut-layouts are shown in Fig. 10. The solid material is blue, the void material, i.e. the cuts, are white. The variations of the stiffness profiles (second row in Fig. 10) and consequently the variations of the geometric parameters (third row) are clearly visible. Note, that the two clamped examples have a solid part at both extremities for fabrication purposes.

The photographs in Fig. 10-bottom finally show the fabricated structures. The viewpoint is here orthogonal to the plane of the silhouettes in order to enable measurements for validation purposes (see details in Sect. 6.3). We constructed supports for all clamped points to enforce the prescribed tangent.
More aesthetic photographs of the final lamp designs are shown in Fig. 11.

6.3. Validation

A direct comparison to a 3D FEM simulation of the entire resulting perforated structure of 1 m length with all its fine geometric details not larger than 3 mm is not possible since it would exceed available computational resources (memory and CPU) of a standard computer. In particular, we would have to simulate a structure of at least 30 million elements to use the same resolution as in the homogenization step, which is a minimum to have

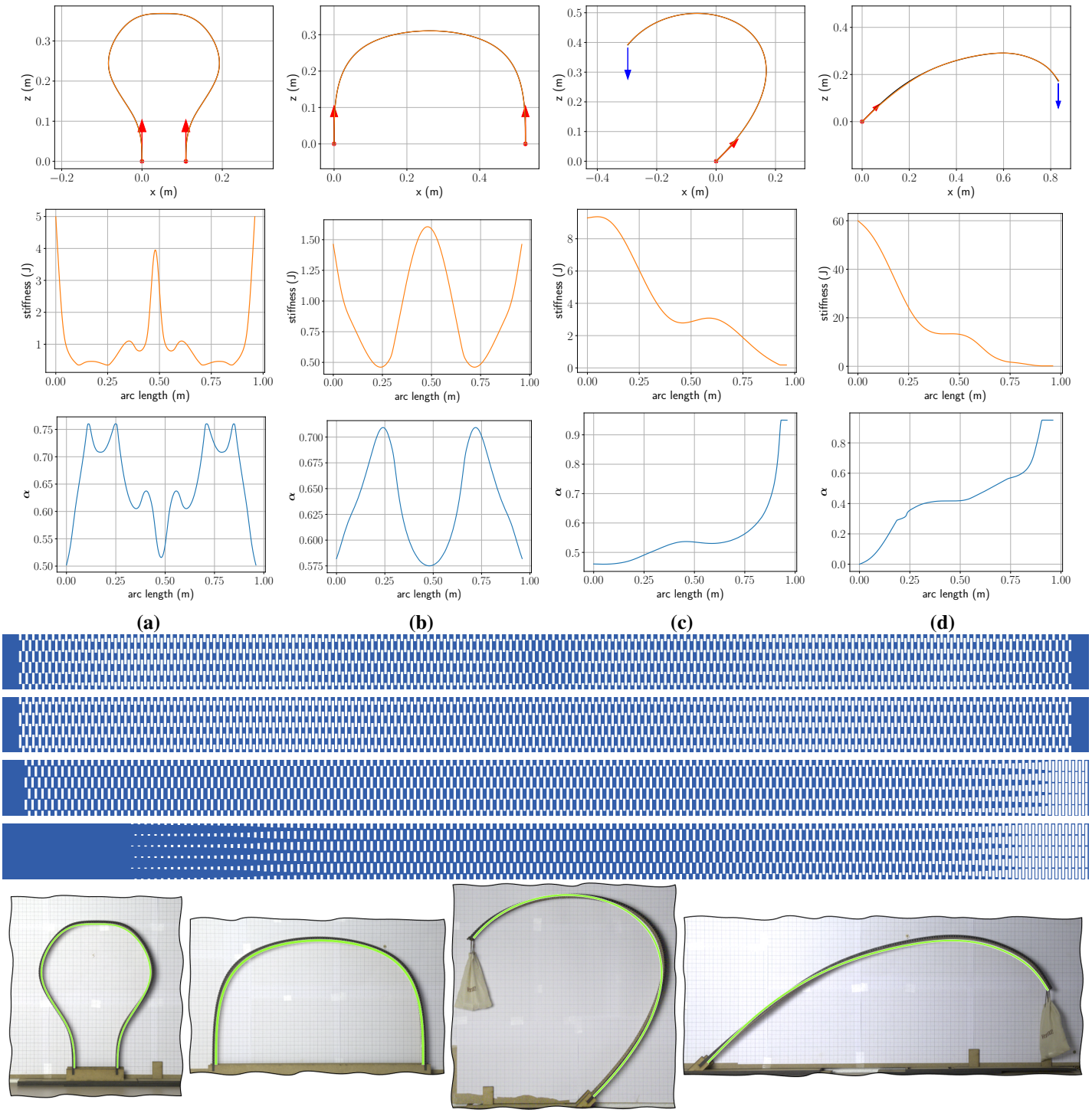

Figure 10: Four fabricated bending-active structures. Input curves with boundary conditions and external loads (first row), Bending stiffness profiles (second row), α (third row). Note that plots have different scales. The blue/white stripes show the cutting patterns, solid is blue, void is white. The bottom row shows the fabricated bending-active structures under loading, with the input curve superimposed (green). Detailed statistics are given in the last 4 rows of Table 1.

sufficiently accurate results. Instead, we performed a visual and quantitative comparison with four fabricated structures. A visual comparison is given in Fig. 10-bottom, where we superposed by hand the optimized silhouette curve $\bar{\mathbf{x}}$ (output of Eq. (10)) with the back-side border of the photographed structure. The back-side curve is visible thanks to the viewpoint of the camera. All fabricated structures fit almost perfectly.

In order to validate quantitatively both the forward simulation and the mechanical models, we computed the average/max Euclidean distance between the silhouette curve of the fabricated models digitized from the photo and the computed solution (scale to same length, equidistant sampling, calibration). The resulting errors are remarkably small, less than 10mm max for one meter length structures, giving a maximum relative error of 10^{-2}, see the last two columns in Table 1.

Name	Boundary conditions	κ_{max} target	Grvty.	$\mathbf{k}_b$ min	$\mathbf{k}_b$ max	#It. mass	#It. inv. design	IPOPT inv. design	Dist.(mm) target-sol. avg / max	Dist.(mm) fabr.-sol. avg / max
ellipse	2p	24.5	no	0.67	7.6	NO	589	5.6s	0.1 / 0.2	-
pentagone w/ reg	2p	40	no	0.19	9.5	NO	4315	12.1s	0.1 / 0.3	-
pentagone w/o reg	2p	40	no	0.19	9.5	NO	4315	47.1s	0.01/ 0.1	-
asymmetrical arch	2p/2t	40	yes	0.19	42.0	4	600	66.5s	0.6 / 2.1	-
triangular arch	2p/2t	12.5	yes	2.20	43.0	2	828	9.5s	0.2 / 0.4	-
heart	2p/2t/mass	56	yes	0.19	55.0	3	16289	171.5s	6.7 /12.3	-
light bulb	2p/2t/mass	6	yes	0.40	5.0	2	1766	21.1s	0.2 / 0.6	3.0 / 7.6
symetrical arch	2p/2t	6.5	yes	0.50	1.6	2	284	3.5s	0.1 / 1.4	1.1 / 2.0
bass clef lamp	1p/1t/mass	6	yes	0.19	9.2	2	892	8.4s	0.1 / 1.3	7.5 /10.7
wall lamp	1p/1t/mass	6	yes	0.19	60.0	2	13340	180.4s	1.3 / 3.7	3.0 / 6.9

Table 1: Statistics of all models. Boundary conditions include fixed points (p), fixed tangents (t), a mass added at one point. Maximal curvature of target shape. Minimal and maximal optimized bending stiffnesses $\mathbf{k}_b$ as output of the inverse design optimization. #It.mass: number of iterations for the iterative mass adjustment algorithm. #It.: number of iterations and timings in seconds for the inverse design problem to converge. Pointwise Euclidean avg/max distances in mm between target and solution. Pointwise Euclidean avg/max distances in mm between target and fabricated structure. All input curves have a length of about 1 m.

Figure 11: Laser-cut bending-active structures made of MDF panels.

7. Conclusion

We presented a computational method to design bending-active structures whose silhouette at equilibrium matched a desired target curve. To this end, we programmed the curvature of the structure thanks to laser-cut rectangular patterns whose sizes were automatically determined using a two-scale algorithm. Our approach, based on the homogenization of the bending properties of the cut MDF wood allowed us to directly play with macro-scale stiffnesses, which in turn allowed us to dramatically reduce the number of design variables and solve our inverse problem using an off-the-shelf optimizer.

While very effective, as demonstrated by our various examples, our tool still presents certain limitations that open the door to exciting future work. For example, we currently fix and keep constant the width of the strips, while the width profile could be given as input by the user to play, e.g., with aesthetics. We also limit the optimization to a single parameter of our cut pattern. Exploring the others, and more generally other parametric families of cuts [49], to improve, e.g., the strength or to play with the appearance of the final structure, in addition to its shape, would be another interesting extension. Finally, it would also be very appealing to generalize our work to 3D, in particular to address the design of 3D developables or surfaces exhibiting low Gaussian curvature, that seem a priori difficult to obtain with methods optimizing ribbons' widths or current state-of-the-art approaches specifically tailored to the design of doubly-curved deployables.

Acknowledgment

This work was supported by the European Unions Horizon 2020 programme under grant agreement No 862025 (FETOpen *ADAM*^{2}). The authors are grateful to Stan Borkowsky and the Amiqual4Home platform for giving us access to their laser-cut machine.

References

[1] J. Lienhard, H. Alpermann, C. Gengnagel, J. Knippers, Active Bending, a Review on Structures where Bending is Used as a Self-Formation Process, International Journal of Space Structures 28 (3-4) (2013) 187–196, doi: \bibinfo{doi}{10.1260/0266-3511.28.3-4.187}.

[2] M. Fleischmann, A. Menges, ICD/ITKE Research Pavilion: A Case Study of Multi-disciplinary Collaborative Computational Design, in: Computational Design Modelling, Springer Berlin Heidelberg, ISBN 978-3-642-23435-4, 239–248, 2012.

[3] F. Laccone, L. Malomo, J. Prez, N. Pietroni, F. Ponchio, B. Bickel, P. Cignoni, FlexMaps Pavilion: a twisted arc made of mesostructured flat flexible panels, Proceedings of IASS Ann. Symposia 2019 (5) (2019) 1–7, ISSN 2518-6582.

[4] N. Kalantar, A. Borhani, Informing Deformable Formworks - Parameterizing Deformation Behavior of a Non-Stretchable Membrane via Kerfing, in: T. Fukuda, W. Huang, P. Janssen, K. Crolla, S. Alhadidi (eds.), Learning, Adapting and Prototyping - Proceedings of the 23rd CAADRIA Conference - Volume 2, Tsinghua University, Beijing, China, 17-19 May 2018, pp. 339-348, CUMINCAD, 1–10, 2018.

[5] C. Hafner, B. Bickel, The Design Space of Plane ElasticCurves, ACM Trans. Graph. 40 (4).

[6] G. Sperl, R. Narain, C. Wojtan, Homogenized yarn-level cloth, ACM Transactions on Graphics (TOG) 39 (4).

[7] B. Bickel, P. Cignoni, L. Malomo, N. Pietroni, State of the Art on Stylized Fabrication, Computer Graphics Forum 37 (6) (2018) 325–342.

[8] A. H. Bermano, T. Funkhouser, S. Rusinkiewicz, State of the Art in Methods and Representations for Fabrication-Aware Design, Comput. Graph. Forum 36 (2) (2017) 509535, ISSN 0167-7055.

[9] J. Vekhter, J. Zhuo, L. F. G. Fandino, Q. Huang, E. Vouga, Weaving Geodesic Foliations, ACM Trans. Graph. 38 (4), ISSN 0730-0301, doi:\bibinfo{doi}{10.1145/3306346.3323043}, URL https://doi.org/10.1145/3306346.3323043.

[10] Y. Ren, J. Panetta, T. Chen, F. Isvoranu, S. Poincloux, C. Brandt, A. Martin, M. Pauly, 3D Weaving with Curved Ribbons, ACM Trans. Graph. 40 (4), ISSN 0730-0301, doi:\bibinfo{doi}{10.1145/3450626.3459788}.

[11] J. Panetta, M. Konaković-Luković, F. Isvoranu, E. Bouleau, M. Pauly, X-Shells: A New Class of Deployable Beam Structures, ACM Trans. Graph. 38 (4), doi:\bibinfo{doi}{10.1145/3306346.3323040}.

[12] S. Pillwein, K. Leimer, M. Birsak, P. Musialski, On Elastic Geodesic Grids and Their Planar to Spatial Deployment, ACM Trans. Graph. 39 (4), doi:\bibinfo{doi}{10.1145/3386569.3392490}.

[13] S. Pillwein, P. Musialski, Generalized Deployable Elastic Geodesic Grids, ACM Trans. Graph. 40 (6), ISSN 0730-0301, doi:\bibinfo{doi}{10.1145/3478513.3480516}.

[14] E. Siéfert, E. Reyssat, J. Bico, B. Roman, Programming stiff inflatable shells from planar patterned fabrics, Soft Matter 16, doi:\bibinfo{doi}{10.1039/D0SM01041C}.

[15] J. Panetta, F. Isvoranu, T. Chen, E. Siefert, B. Roman, M. Pauly, Computational Inverse Design of Surface-based Inflatables, ACM Trans. Graph. .

[16] L. Malomo, J. Pérez, E. Iarussi, N. Pietroni, E. Miguel, P. Cignoni, B. Bickel, FlexMaps: Computational Design of Flat Flexible Shells for Shaping 3D Objects, ACM Trans. Graph. 37 (6), doi:\bibinfo{doi}{10.1145/3272127.3275076}.

[17] A. Garg, A. O. Sageman-Furnas, B. Deng, Y. Yue, E. Grinspun, M. Pauly, M. Wardetzky, Wire Mesh Design, ACM Trans. Graph. 33 (4), doi:\bibinfo{doi}{10.1145/2601097.2601106}.

[18] M. Konaković, K. Crane, B. Deng, S. Bouaziz, D. Piker, M. Pauly, Beyond Developable: Computational Design and Fabrication with Auxetic Materials, ACM Trans. Graph. 35 (4), doi:\bibinfo{doi}{10.1145/2897824.2925944}.

[19] P. Celli, C. McMahan, B. Ramirez, A. Bauhofer, C. Naify, D. Hofmann, B. Audoly, C. Daraio, Shape-morphing architected sheets with non-periodic cut patterns, Soft Matter 14, doi:\bibinfo{doi}{10.1039/C8SM02082E}.

[20] T. Chen, J. Panetta, M. Schnaubelt, M. Pauly, Bistable Auxetic Surface Structures, ACM Trans. Graph. .

[21] A. Derouet-Jourdan, F. Bertails-Descoubes, J. Thollot, Floating tangents for approximating spatial curves with G1 piecewise helices, Computer Aided Geometric Design 30 (5) (2013) 490–520, ISSN 0167-8396, doi:\bibinfo{doi}{https://doi.org/10.1016/j.cagd.2013.02.007}.

[22] F. Bertails-Descoubes, A. Derouet-Jourdan, V. Romero, A. Lazarus, Inverse design of an isotropic suspended Kirchhoff rod: theoretical and numerical results on the uniqueness of the natural shape, Proceedings of the Royal Society A: Mathematical, Physical and Engineering Sciences 474 (2212), doi:\bibinfo{doi}{10.1098/rspa.2017.0837}.

[23] J. Pérez, B. Thomaszewski, S. Coros, B. Bickel, J. A. Canabal, R. Sumner, M. A. Otaduy, Design and Fabrication of Flexible Rod Meshes, ACM Trans. Graph. 34 (4), doi:\bibinfo{doi}{10.1145/2766998}.

[24] M. Liu, L. Domino, D. Vella, Tapered elasticæ as a route for axisymmetric morphing structures, Soft Matter 16, doi:\bibinfo{doi}{10.1039/D0SM00714E}.

[25] J. Panetta, Q. Zhou, L. Malomo, N. Pietroni, P. Cignoni, D. Zorin, Elastic Textures for Additive Fabrication, ACM Trans. Graph. 34 (4), doi:\bibinfo{doi}{10.1145/2766937}.

[26] D. C. Tozoni, J. Dumas, Z. Jiang, J. Panetta, D. Panozzo, D. Zorin, A Low-Parametric Rhombic Microstructure Family for Irregular Lattices, ACM Trans. Graph. 39 (4), ISSN 0730-0301, doi:\bibinfo{doi}{10.1145/3386569.3392451}.

[27] C. Schumacher, B. Bickel, J. Rys, S. Marschner, C. Daraio, M. Gross, Microstructures to Control Elasticity in 3D Printing, ACM Trans. Graph. 34 (4), doi:\bibinfo{doi}{10.1145/2766926}.

[28] B. Zhu, M. Skouras, D. Chen, W. Matusik, Two-Scale Topology Optimization with Microstructures, ACM Trans. Graph. 36 (4), ISSN 0730-0301, doi:\bibinfo{doi}{10.1145/3072959.3095815}.

[29] K. Leimer, P. Musialski, Reduced-Order Simulation of Flexible Meta-Materials, in: Symposium on Computational Fabrication, SCF '20, 1–11, doi:\bibinfo{doi}{10.1145/3424630.3425411}, 2020.

[30] C. Schumacher, S. Marschner, M. Gross, B. Thomaszewski, Mechanical Characterization of Structured Sheet Materials, ACM Trans. Graph. 37 (4), ISSN 0730-0301, doi:\bibinfo{doi}{10.1145/3197517.3201278}.

[31] Y. Zhang, Z. Yan, K. Nan, D. Xiao, Y. Liu, H. Luan, H. Fu, X. Wang, Q. Yang, J. Wang, W. Ren, H. Si, F. Liu, L. Yang, H. Li, J. Wang, X. Guo, H. Luo, L. Wang, Y. Huang, J. A. Rogers, A mechanically driven form of Kirigami as a route to 3D mesostructures in micro/nanomembranes, Proceedings of the National Academy of Sciences 112 (38), doi:\bibinfo{doi}{10.1073/pnas.1515602112}.

[32] Z. Liu, H. Du, J. Li, L. Lu, Z.-Y. Li, N. X. Fang, Nano-kirigami with giant optical chirality, Science Advances 4 (7), doi:\bibinfo{doi}{10.1126/sciadv.aat4436}.

[33] A. Rafsanjani, K. Bertoldi, Buckling-Induced Kirigami, Physical Review Letters 118, doi:\bibinfo{doi}{10.1103/PhysRevLett.118.084301}.

[34] A. Rafsanjani, L. Jin, B. Deng, K. Bertoldi, Propagation of pop ups in kirigami shells, Proceedings of the National Academy of Sciences 116 (17), doi:\bibinfo{doi}{10.1073/pnas.1817763116}.

[35] G. Brth, Boxdesigner Galerie (visited on 04/02/2022), ????

[36] J. Sliseris, H. Andrae, M. Kabel, B. Dix, B. Plinke, O. Wirjadi, G. Frolovs, Numerical prediction of the stiffness and strength of medium density fiberboards, Mechanics of Materials 79, doi:\bibinfo{doi}{10.1016/j.mechmat.2014.08.005}.

[37] J. Bonet, R. D. Wood, Nonlinear Continuum Mechanics for Finite Element Analysis, Cambridge University Press, 2 edn., doi:\bibinfo{doi}{10.1017/CBO9780511755446}, 2008.

[38] C. Geuzaine, J.-F. Remacle, Gmsh: a three-dimensional finite element mesh generator with built-in pre- and post-processing facilities, International Journal for Numerical Methods in Engineering 79 (11).

[39] M. S. Alnæs, J. Blechta, J. Hake, A. Johansson, B. Kehlet, A. Logg, C. Richardson, J. Ring, M. E. Rognes, G. N. Wells, The FEniCS Project Version 1.5, Archive of Numerical Software 3 (100), doi:\bibinfo{doi}{10.11588/ans.2015.100.20553}.

[40] B. Audoly, Y. Pomeau, Elasticity and geometry: from hair curls to the nonlinear response of shells, Oxford University Press, 2010.

[41] M. Bergou, M. Wardetzky, S. Robinson, B. Audoly, E. Grinspun, Discrete Elastic Rods, in: ACM SIGGRAPH 2008 Papers, Association for Computing Machinery, New York, NY, USA, ISBN 9781450301121, doi:\bibinfo{doi}{10.1145/1399504.1360662}, URL https://doi.org/10.1145/1399504.1360662, 2008.

[42] A. Wchter, L. T. Biegler, On the implementation of an interior-point filter line-search algorithm for large-scale nonlinear programming, Mathematical Programming 106 (1) (2006) 25–57, ISSN 1436-4646, doi:\bibinfo{doi}{10.1007/s10107-004-0559-y}.

[43] G. P. A. Bensoussan, J.L. Lions, Asymptotic Analysis for Periodic Structures, North-Holland, Amsterdam, 1978.

[44] G. Guedes, N. Kikuchi, Preprocessing and postprocessing for materials based on the homogenization method with adaptive fini, Comput. Meth. Appl. Mech. Eng. 83 (1990) 142–198.

[45] E. M. Arkin, L. P. Chew, D. P. Huttenlocher, K. Kedem, J. B. M. Mitchell, An efficiently computable metric for comparing polygonal shapes, IEEE Trans. Pattern Anal. Mach. Intell. 13 (1990) 209–216.

[46] R. Veltkamp, Shape matching: similarity measures and algorithms, in: Proceedings International Conference on Shape Modeling and Applications, 188–197, doi:\bibinfo{doi}{10.1109/SMA.2001.923389}, 2001.

[47] T. Gatzke, C. Grimm, M. Garland, S. Zelinka, Curvature maps for local shape comparison, in: International Conference on Shape Modeling and Applications 2005 (SMI' 05), 244–253, doi:\bibinfo{doi}{10.1109/SMI.2005.13}, 2005.

[48] R. Vergne, P. Barla, G.-P. Bonneau, R. Fleming, Flow-Guided Warping for Image-Based Shape Manipulation, ACM Transactions on Graphics 34 (4) (2016) Article No. 93, doi:\bibinfo{doi}{10.1145/2897824.2925937}.

[49] S. Zarrinmehr, M. Ettehad, N. Kalantar, A. Borhani, S. Sueda, E. Akleman, Interlocked archimedean spirals for conversion of planar rigid panels into locally flexible panels with stiffness control, Computers & Graphics 66 (2017) 93–102, ISSN 0097-8493, doi:\bibinfo{doi}{https://doi.org/10.1016/j.cag.2017.05.010}, Shape Modeling International 2017.